Direct Observation of Mass Oscillations due to Ablative Richtmyer-Meshkov Instability and Feedout in Planar Plastic Targets

Y. Aglitskiy

Science Applications International Corporation, McLean, VA 22150

A. L. Velikovich, M. Karasik, V. Serlin, C. J. Pawley, A. J. Schmitt, S. P. Obenschain, A. N. Mostovych

Plasma Physics Division, Naval Research Laboratory, Washington, DC 20375

J. H. Gardner

Laboratory for Computational Physics and Fluid Dynamics, Naval Research Laboratory, Washington, DC 20375

N. Metzler

Science Applications International Corporation, McLean, VA 22150

Abstract

Perturbations that seed Rayleigh-Taylor (RT) instability in laser-driven targets form during the early-time period. This time includes a shock wave transit from the front to the rear surface of the target, and a rarefaction wave transit in the opposite direction. During this time interval, areal mass perturbations caused by all sources of non-uniformity (laser imprint, surface ripple) are expected to oscillate. The first direct experimental observations of the areal mass oscillations due to ablative Richtmyer-Meshkov (RM) instability and feedout followed by the RT growth of areal mass modulation are discussed. The experiments were made with 40 to 99 μm thick planar plastic targets rippled either on the front or on the rear with a sine wave ripple with either

30 or 45 μm wavelength and with 0.5, 1 or 1.5 μm amplitude. Targets were irradiated with 4 ns long Nike KrF laser pulses at ~50 TW/cm^2. The oscillations were observed with our novel diagnostic technique, a monochromatic x-ray imager coupled to a streak camera. For the ablative RM instability (front side ripple), the mass modulation amplitude was typically observed to grow, reach a peak, and then decrease, after which the exponential RT growth started. In some cases, one phase reversal due to the ablative RM instability was observed. For the feedout geometry (rear side ripple), in all cases two phase reversals were observed: a distinct half-oscillation was followed by the onset of the RT growth, resulting in a second phase reversal.

PACS numbers: 52.57.Fg, 52.70.La, 47.20.-k

I. Introduction

The success of the laser fusion program in general,[1,2] and of its flagship NIF project in particular (including its indirect-[3] and direct-drive[4] ignition options), is critically dependent on our ability to simulate target performance. We have to rely upon simulations to predict whether or not a target irradiated on a large-scale facility will actually ignite. Thus, while a large-scale facility is being constructed,[5] smaller facilities are used to keep testing and improving the reliability of our codes. In particular, they should be fully validated and benchmarked vs. experiment in a single-mode regime.

Target distortion due to the Rayleigh-Taylor (RT) instability has long been identified as a critical issue of the laser fusion program. Growth rates of the RT instability have been measured in numerous experiments starting from the mid-1980s (see Refs. 6-10 and references therein). However, little experimental data is available on the important processes that form the initial seeds for the RT perturbation modes. All sources of non-uniformity - laser imprint and beam imbalance, roughness of the outer and inner surfaces of the target– contribute to the RT seeding process. Seeding takes place during the so-called "early-time" period that includes a shock wave transit from the front to the rear surface of the target, and a rarefaction wave transit in the opposite direction. If the driving laser intensity is nearly constant, then at the early time the target is not accelerated, and there is no exponential RT growth at the ablation front. Nevertheless, as noted in Ref. 11 (see also the discussion in Refs. 12-15), one might expect some linear in time, Richtmyer-Meshkov (RM)-like[13] growth to proceed as long as there is no acceleration and the perturbation amplitudes are small. Indeed, at the very beginning of the "early-time" phase a linear growth takes place. However, this is not an

unlimited growth characteristic of the classical RM instability, but rather an early phase of an oscillatory process. Simulations and theory indicate that during this early time the areal mass perturbations oscillate rather than grow.[12-17] The physical mechanisms driving the oscillations are different, depending on whether the perturbations are initially at the front surface of the target (laser imprint, front surface roughness) or at its rear surface (feedout). The oscillations are caused in the former case by the "rocket effect" due to mass ablation,[15, 19] and in the latter case by a lateral mass redistribution in a rippled rarefaction wave.[18] The subsequent RT growth for each mode starts at the amplitude and phase determined by this oscillatory process. To ensure that not only the growth rates, but also the actual amplitudes of the perturbation modes are simulated correctly, we need to fully understand and be able to observe and model the early-time oscillations.

These mass oscillations have been observed for the first time in the experiments carried out on the Nike KrF laser facility at the Naval Research Laboratory in 2000-2001. To make the observations possible, we developed a novel diagnostic technique by coupling a streak camera to the Nike monochromatic high-resolution x-ray imaging system.[20] Our first observations of the oscillations due to the ablative RM instability and feedout have recently been reported in Refs. 21 and 22, respectively.

This article describes in detail our experimental data on the early-time areal mass oscillations due to both the ablative RM instability and feedout. Section II outlines the theory and presents the requirements for the laser driver and for the diagnostic system that must be satisfied to make the observation of the oscillations possible. Section III describes our diagnostics and the experimental setup and presents the experimental data and some of the simulation results. Section IV concludes with a discussion.

II. Theory

When the irradiated front surface of the target is rippled, the oscillatory behavior during the shock-rarefaction transit time is caused by the so-called ablative Richtmyer-Meshkov instability. These oscillations have been first predicted in our simulations,[12] and then explained by the theory of Ref. 15 (where the term "ablative RM instability" was introduced), and later confirmed by many other simulations,[16, 17] but only very recently have been observed experimentally for the first time.[21] The frequency of these decaying oscillations of ablation front is consistent with the recently established expression[19, 23] for the growth rate Γ_a of the ablative RT instability at high Froude number (low acceleration):

$$\Gamma_a \cong \left(gk - \frac{1}{r_D} k^2 v_a^2 \right)^{1/2} - 2kv_a , \qquad (1)$$

Here g is the acceleration, $r_D << 1$ is the effective blowoff-plasma-to-ablation-front density ratio, $v_a = \dot{m} / r_s$ is the ablation velocity ($\dot{m}$ is the mass ablation rate, r_s is the shock-compressed target density), and r_D is estimated for a given perturbation wavelength $l = 2p / k$ by the formulas given in Ref. 23. The main difference between (1) and all the versions of the Bodner-Takabe formula[24] (see also references in Refs. 1, 2, 23) is the presence of the negative term under the square root. The so-called "rocket effect" described by this term emerges because, as noted in Ref. 24, the ablation front is an isotherm. When it is perturbed, and a part of it gets closer to the hot laser absorption zone, the temperature at the ablation front does not increase, but the temperature gradient in its vicinity, ∇T, does. This in turn increases the local heat flux to the ablation front, $-k\nabla T$, and hence the rate of mass ablation from it, thereby increasing the ablative

pressure and pushing this part of the ablation front away from the laser absorption zone. The physics of this "rocket effect" is explained in detail in Refs. 15, 17, 19. This "rocket effect" rather than the mass flow through the ablation front determines the cut-off wavelength of ablative RT instability at high Froude numbers. Formula (1) giving the rate of exponential growth[19, 23] is formally applicable even below the cut-off wavelength, i. e. when the acceleration is low, or the wavelength is short, and such a growth does not take place.[15, 16] In the latter case, the imaginary part represents the frequency of decaying oscillations. If we substitute the value of $g = 0$, appropriate for the shock-rarefaction transit time, into (1), then the contribution of the square root term is purely imaginary, $\mathrm{Im}\,\Gamma_a = \pm\Omega_a$, where

$$\Omega_a \cong k v_a / r_D^{1/2} \tag{2}$$

is the estimated oscillation frequency.[15]

Formulas (1)-(2) refer to the oscillations of a rippled ablation front. These are not directly measured by our face-on diagnostics. The observed total modulation of areal mass includes additionally the two distinct oscillatory contributions, which we combine below into a single term, dm_{shock}: the rippled shock front and the mass non-uniformity due to the entropy and sonic perturbations in the shocked plasma between the ablation front and the shock front,

$$dm_{total} = dm_a + dm_{sf} + \int_{x_a}^{x_{sf}} dr \;\; dx \equiv dm_a + dm_{shock}\,, \tag{3}$$

where the subscripts "*a*" and "*sf*" refer to the ablation front and the shock front, respectively. The dm_a component is a perturbation localized near the accelerated surface, which provides the initial conditions for the subsequent RT growth once the target starts

to accelerate. On the contrary, the dm_{shock} component is partly localized near the stable shock front, partly spread over the plasma volume between the shock and ablation fronts, and does not directly participate in triggering the RT growth.

In Figure 1(a), these contributions are shown separately, as given by the analytical small-amplitude theory,[13] where at the ablation front the Sanz-Piriz boundary conditions[19] are satisfied. The figure is plotted for the parameters characteristic of a plastic target ($r_0 = 1.07$ g/cm^3) irradiated with a KrF laser ($l_L = 0.248$ μm) at ~50 TW/cm^2: $v_a = 10^5$ cm/s, constant shock velocity $D = 4\times10^6$ cm/s. Here, the perturbation wavelength is $l = 30$ μm, the corresponding value of $r_D = 0.09$, and the ideal gas equation of state with $g = 5/3$ is assumed. The areal mass modulation amplitudes *dm* are expressed in units of $dm_0 = r_0 a_0$, where r_0 is the initial density, a_0 is the initial ripple amplitude. Figure 1(a) demonstrates that the contribution to the total mass variation due to the rippled ablation front, dm_a, becomes the dominant one after a relatively short transitional period, ~0.8 ns. During this period, the observed growth of dm_{total} is caused by comparable contributions of the increasing ablation front term, dm_a, and the decreasing shock term, dm_{shock}, which has a different sign. Later, the contribution of the shock term reduces to small, slowly decaying sonic oscillations. For the above conditions, Eq. (2) estimates the half-period of the ablative RM oscillations as 4.5 ns, in agreement with Fig. 1(a), where the oscillation cycle starts somewhere in the middle. The frequency of the shock-induced sonic oscillations is

$$\Omega_s = c_s k = \frac{2p\left[g\,(R-1)\right]^{1/2} D}{R\,l}, \qquad (4)$$

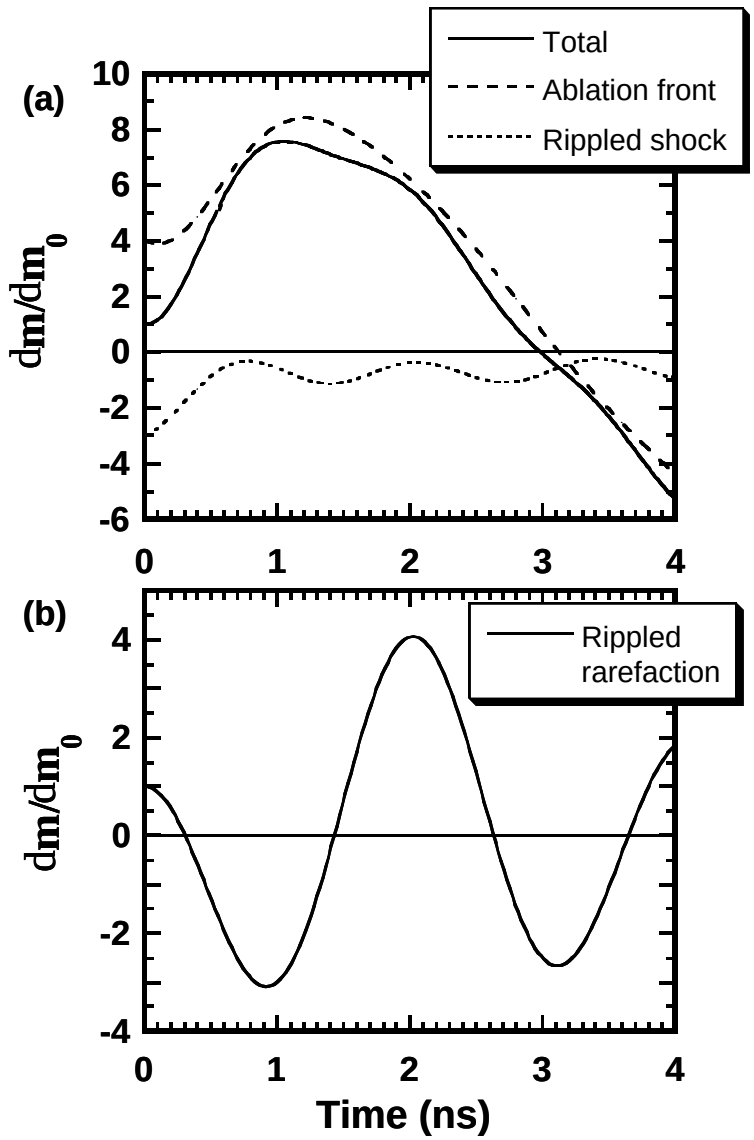

Fig. 1. Time history of areal mass modulation amplitude predicted by analytical small-amplitude theory for a plastic target rippled with $l = 30$ μm on (a) the front side and (b) on the rear side. The origin of time $t = 0$ corresponds to the instant when (a) a shock wave propagating at constant velocity $D = 4\times10^6$ cm/s is launched at the front side; and (b) when such a shock wave breaks out at the rear side. (a) The total mass modulation dm_{total} and contributions to it due to the perturbed ablation front dm_a and to the rippled shock front and post-shock flow dm_{shock} are shown by solid, dashed, and dotted lines, respectively.

where c_s is the post-shock speed of sound, R is the shock compression ratio. The adiabatic exponent g and R enter (4) separately, as the ideal gas equation of state might only be applicable to the target material when it expands after the shock passage.[25] For the above parameter values (R = 4, g = 5/3), (4) yields the half-period of 0.7 ns, again in agreement with Fig. 1(a), and almost an order of magnitude less than that given by Eq. (2). Figure 1(a) shows that the negative contribution of dm_{shock} shifts the times of peak amplitude and phase reversal of dm_{total} to slightly earlier values compared to those characteristic of dm_a: i. e., dm_{total} peaks and changes its phase earlier than dm_a by 0.2 ns and 0.15 ns, respectively.

Note another important difference between the oscillatory contributions to dm_{total} from the ablation front and the shock front. As demonstrated by Figure 1(a), the decaying shock-induced oscillations cannot change the phase of the mass variation (except at a very late time, not shown in the figure, when the corresponding amplitude of oscillations becomes negligible[22]). On the contrary, the oscillations of the ablation front lead to an actual phase reversal [in Fig. 1(a), at about 3 ns], after which the modulation amplitude increases again, overshooting its initial value. In other words, a change of phase of mass modulation observed during the shock-rarefaction transit time could only be attributed to the ablative RM oscillations.

Therefore, to observe a half-cycle of ablative RM oscillations (i. e. to see the mass modulation reach its peak and then decrease below zero), we need to make the shock-rarefaction transit time long enough to allow its contribution to become dominant.

Comparing Fig. 1(a) with Eq. (2) (phase reversal at 3 ns, estimated half-period 4.5 ns), we see that the required long transit time is roughly translated into ~1/3 of the oscillation period. Therefore, the following two conditions must be satisfied. (a) The driving laser pulse duration, t_L, should be longer than $(1/3)\times 2p/\Omega_a$ [cf. Fig. 1(a)], which leads to the condition

$$t_L > \frac{l r_D^{1/2}}{3v_a}. \tag{5}$$

(b) The target should be sufficiently thick, so that the oscillation half-cycle completes before the rarefaction wave from the rear side of the target breaks out at its front side, triggering the RT growth. The rarefaction breakout time could be estimated as

$$t_{rb} = (1+\tilde{M}_0)\frac{L}{D} \cong 1.5\times\frac{L}{D}, \tag{6}$$

where L is the initial thickness of the target, D is the velocity of the shock wave driven into the target, $\tilde{M}_0 < 1$ is the Mach number characteristic of the shocked fluid flow with respect to the shock front[18] (in this estimate, we assumed $\tilde{M}_0 \cong 0.5$, close to the value $\tilde{M}_0 = 1/\sqrt{5} = 0.45$ found for a strong shock in an ideal gas with g = 5/3). Therefore the target thickness L should satisfy the condition

$$L > \frac{2Dr_D^{1/2}}{9v_a} l . \tag{7}$$

For a relatively short perturbation wavelength $l = 30$ μm, we find from (5) and (7): $t_L > 3$ ns, $L > 80$ μm. When the conditions (5), (7) are approached but not exactly met, one can expect to see a little more than a quarter of the RM oscillation: the mass modulation reaches its peak and starts decreasing. E. g., for the parameters of the

GEKKO-XII experiment[26] ($l_L = 0.53\,\mu$m, ~40 TW/cm^2, $l \geq 60$ μm), one finds from (5) that a 2.2 ns laser pulse duration is only sufficient for the mass modulation growth to slow down, approaching its first peak, as observed.

When the reflected rarefaction wave breaks out, the ablation front starts to accelerate. The onset of the exponential RT growth occurs about $\Delta t_{RT} = 1/\Gamma$ later than the start of acceleration, where Γ is the linear RT growth rate. To estimate Δt_{RT} from below, we assume the classical expression for $\Gamma = (gk)^{1/2} = (2pp_s / l\, r_0 L)^{1/2}$, where p_s is the post-shock pressure, which yields

$$\Delta t_{RT} = \frac{1}{D}\left[\frac{RL\,l}{2p\,(R-1)}\right]^{1/2}. \qquad (8)$$

For the parameters of the above example and L = 60 μm, we obtain: $\Delta t_{RT} = 0.5$ ns. Then the mass modulation amplitude, having passed either through a minimum or through a phase reversal, starts growing again.

When the rear side of the target is rippled, the oscillations are caused by a different mechanism.[18] The planar shock wave launched at the front side first reaches the valleys of the rippled rear side, where the target material starts to decompress, while the high post-shock pressure is maintained near the peaks. The lateral pressure gradient in a reflected rippled rarefaction wave drives the mass from the peaks to the valleys. Shortly, the lateral mass flow reverses the phase of mass modulation: more mass is collected (less mass is left) where the valleys (the peaks) were initially located. At the same time, a reversed pressure gradient builds up, slowing down the lateral mass flow. The mass modulation amplitude reaches its peak at reversed phase and starts decreasing; after a while, its phase is reversed for the second time, and there is again more mass at the initial

location of the peaks. The decaying oscillations of areal mass in a rippled rarefaction wave continue until its leading edge breaks out at the front side of the target. Then the acceleration begins, and, after Δt_{RT}, the exponential RT growth follows.

The areal mass oscillations in a rippled rarefaction wave predicted by the small-amplitude analytical theory of Ref. 18 are shown in Fig. 1(b). Here, all the parameters are the same as in Fig. 1(a) except the origin of time corresponds to the shock breakout at the rippled rear surface of the target. Comparing Fig. 1(b) to Fig. 1(a), we observe the oscillation frequency in a rippled rarefaction wave to be lower than that of the shock-induced oscillations given by (4). This is because the temperature of the plasma expanding in a rarefaction wave decreases below its post-shock value, and so does the mass-averaged speed of sound. A rough estimate of the corresponding oscillation frequency Ω_r is[18]

$$\Omega_r = \left[\frac{2(g-1)}{g+1}\right]^{(g-1)/(3-g)} \Omega_s , \qquad (9)$$

where Ω_s is given by (4). For $g = 5/3$ we find: $\Omega_r = \Omega_s / \sqrt{2}$, implying the oscillation half-period 0.95 ns, in agreement with Fig. 1(b). The amplitude of the areal mass oscillations in a rippled rarefaction wave, however, is much higher compared to those induced by a rippled shock wave. A rippled rarefaction wave can produce multiple observable phase reversals, provided that the rarefaction transit time is sufficiently long. To put it differently, these oscillations are observable if the target thickness L is not too small compared to the perturbation wavelength l.

The corresponding conditions derived from the general formulas of Ref. 18, are presented below for the same parameters as above (plastic, R = 4, g = 5/3) The first phase

reversal of mass modulation, which in Fig. 1(b) occurs at 0.3 ns after the shock breakout, is observable if

$$L > 0.9 \times l \ . \tag{10}$$

The mass modulation in a rippled rarefaction wave reaches its first negative peak [in Fig. 1(b), at 0.9 ns after the shock breakout] if

$$L > 2.7 \times l \ . \tag{11}$$

The corresponding condition on the laser pulse duration clearly is

$$t_L > t_{rb} \ , \tag{12}$$

where t_{rb} is given by (6). When even the condition (10) is not satisfied, as in the experiment of Ref. 27 (L = 25 μm, l = 100 μm), there is not enough time for the feedout-related areal mass oscillations to occur, and the long-wavelength theory[28] is applicable. In the indirect-drive feedout experiment[29] (Al foil targets rippled on the rear side, l = 50 μm), the condition (10) is not satisfied only for a thin target (L = 35 μm). Indeed, for a thin target both the experiment and the simulation of Ref. 29 showed no phase reversal. Rather, a dip in the mass variation amplitude immediately after the shock breakout was detected, which was, of course, the beginning of the oscillation. For their intermediate (L = 50 μm) and thick (L = 85 μm) targets the condition (10) was satisfied with considerable margin. In agreement with (10), for the thick target the first phase reversal of mass modulation had been both observed and simulated.[29] For the intermediate target it was predicted in their simulation but not observed in the experiment.[29]

All the targets used in our feedout experiments (l = 30 to 45 μm, L = 40 to 60 μm) satisfied (10) but not (11). Consequently, the mass modulation was expected to always reverse its phase but not reach the maximum value predicted for the rippled

rarefaction wave, about 3 times the initial amplitude.[18] Before this could happen, the leading edge of the rippled rarefaction wave breaks out at the front side of the target, starting the RT growth. The reflected rarefaction wave is first emitted from the valleys, then from the peaks, and propagates at the same velocity, equal to the post-shock speed of sound. Hence its leading edge first breaks out at the front side just opposite the valleys, where the target is thinner, and its areal mass initially lower.[27, 28] These parts of the target are the first to start accelerating, and the RT mechanism immediately begins turning them into bubbles, further decreasing the areal mass at these locations, dumping the mass from there into the spikes that trail behind. This growth of mass modulation thus occurs in phase with the initial rear-surface ripples: the initially thin (thick) parts of the target become thinner (thicker). Since the inequality (10) is satisfied, the RT growth starts when the phase of total mass modulation in the volume of the target is reversed. Therefore, the RT growth has to compete against the lateral mass flow in the rippled rarefaction wave. Being exponential, the RT growth in most cases takes over shortly after its onset, see (8). Then the absolute value of mass modulation starts decreasing, reverses its phase again and continues to grow at its initial phase. We conclude that when the conditions (10) and (12) are satisfied, the mass modulation is expected to decrease, reverse its phase, increase and reach a peak at negative phase, then decrease again, exhibit a second phase reversal and continue to grow.

The above conditions are quite restrictive. The experiments must be made with long laser pulses, thick targets, and relatively short perturbation wavelengths. Moreover, the oscillating perturbation amplitudes to be observed most of the time remain quite small, of the order of their initial values. It should be noted, however, that one important

requirement can be relaxed in comparison with experiments[6-10] where the RT growth is measured. The initial perturbation amplitude a_0 does not have to be very small compared to the perturbation wavelength; the values of ka_0 up to 0.4 are acceptable, thus facilitating the observation. During the early-time period higher harmonics experience damped oscillation rather than unlimited growth, just as the fundamental, with the higher modes decaying faster. Consequently, they do not overtake the fundamental mode, and the observed oscillations are essentially linear in perturbation amplitude up to much higher values of ka than in the cases of either exponential RT or linear classical RM interfacial growth.

III. Experiment

A. Experimental setup

Our experiments were performed with the Nike KrF laser[30] (l_L = 248 nm). The laser radiation in 37 overlapping beams was focused to a spot 750 μm FWHM in diameter, with a flat central region 400 μm in diameter. Most of our experiments were made at intensities ~50 TW/cm^2. The length of the main Nike pulse is 4 ns. From equations (5), (6), (10), (12) we find that this is long enough both to complete a half-cycle of the ablative RM oscillations and to reach the inverted peak of the mass oscillation in a rippled rarefaction wave before its breakout, provided that the perturbation wavelength l is not greater than about 40 μm. We used rippled planar plastic targets with l = 30 and 45 μm and peak-to-valley amplitudes $2a_0$ from 1 to 3 μm. Target thickness was 40-99 μm for RM and 40-60 μm for feedout experiments. The highly smooth profile[30] of the Nike laser ensured that laser-imposed perturbations were negligible compared to the target ripple.

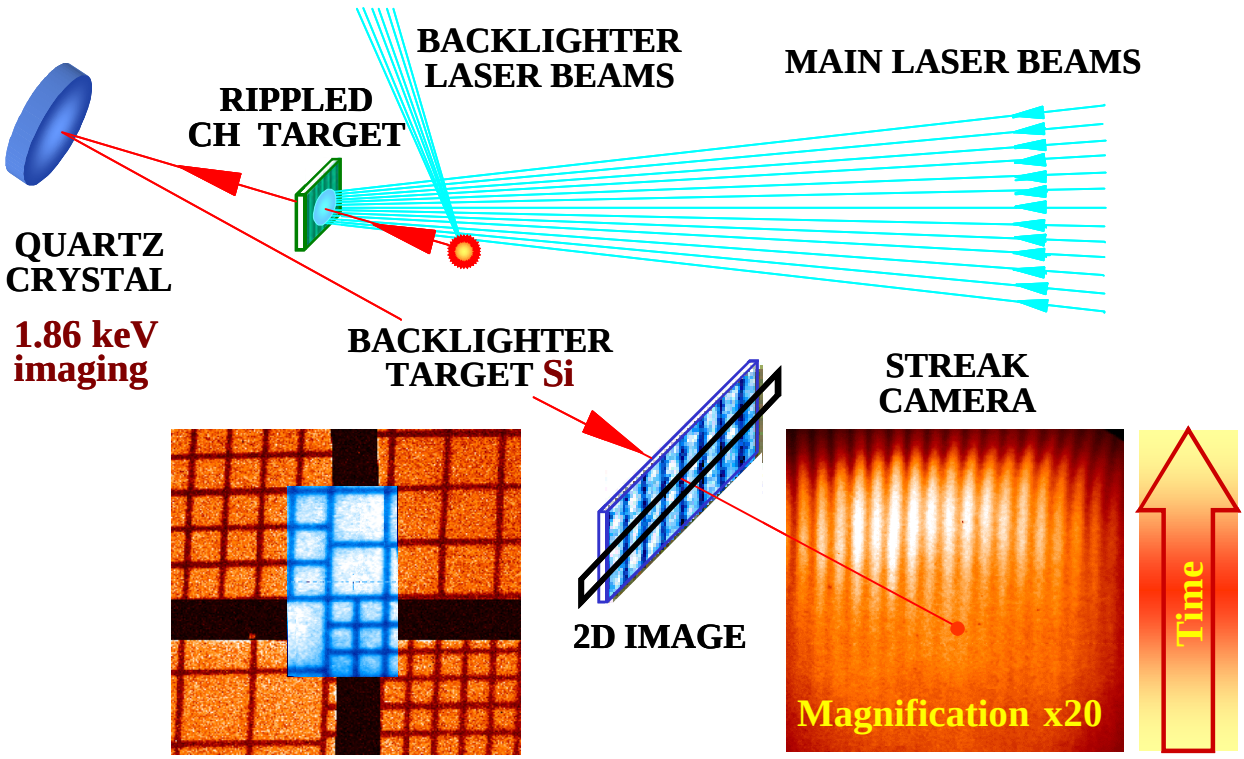

Fig. 2. The general scheme of the experiment. Also shown are: (a) Test images of a 150-to-400 lpi composite mesh obtained on x-ray film (quadrants) and on the open photocathode of the streak camera (insert in the middle); wires of 7 μm width are clearly seen on both images, though the streak camera image obviously has less spatial resolution; (b) An actual streak record showing the RT growth of areal mass modulation – peaks and valleys are more pronounced at late time. Four-quadrant composite mesh was used for pointing the focal spot onto the streak camera slit with an accuracy of 20-30 μm.

We used backlighting and a monochromatic x-ray imaging system based on Bragg reflection from spherically curved crystals[31] to observe the evolution of target mass perturbations. X-ray imaging using curved crystals has been successfully used on the NRL Nike KrF laser for the past five years.[20, 32, 33] Compared to other x-ray imaging techniques like pinholes, Kirkpatrick-Baez microscopes, and Fresnel lenses, a curved crystal imager has several advantages. It is a high throughput, high spatial resolution and, by nature, monochromatic diagnostic technique, all at the same time. Previously, the curved crystal imager has been used at NRL in combination with a framing camera to provide sequences of high spatial resolution still images (up to four snapshots that correspond to four different times) taken with a time resolution of 200 ps.[32] This diagnostic technique is fully adequate when the observed mass non-uniformity varies monotonically in time, e. g., during the fast RT growth.[32, 33]

Observation of the oscillating mass modulation presents a new challenge to the imaging diagnostics because of the essentially non-monotonic evolution of the processes under study. In these cases, the diagnostics that record a limited number of images incrementally over a relatively long period of time are difficult to apply: it is easy to lose important information or even completely miss the effect. The number of snapshots can only be increased by adding more crystal-backlighter pairs, which is technically difficult to the point of unfeasibility. To extend the capabilities of our diagnostic technique, we modified the Nike imaging diagnostic setup by adding a streak camera to the system, which made it possible to analyze continuous time behavior of x-ray images.

The diagnostic setup is presented in Fig. 2. Approximately 500 J is delivered to a silicon backlighter target, producing x-rays that backlight the main target for about 5 ns.

The spherically curved quartz crystal selects the resonance line of the He-like Si ($hn = 1.86$ keV) and projects a 2-D monochromatic image of the target on the entrance slit of an x-ray streak camera. The spatial resolution is retained in one relevant direction, i. e. along the wave vector of the ripple on the target surface, producing 1-D streak records. In addition to being capable of obtaining qualitatively different experimental results, the new modified system can do it using just one crystal and one backlighter. A somewhat similar setup with a thin slit as an imaging device has been used at NRL in 1987 for pioneering measurements of the RT growth rates.[6]

We used a quartz crystal with the cut 1011 and radius of curvature of 200 mm. With 1.86 keV probing energy, we were able to study up to ≈100 μm thick plastic (CH) targets rippled with perturbation wavelength l = 30 or 45 μm from either the front or the rear side. The streak records were taken with a time resolution of 170 ps, which is sufficient for the 0.5 ns characteristic times of interest. The large field of view (500 μm) combined with the large flat top (400 μm) of the laser focal spot gave us more ripples available for Fourier transform analysis, thus ensuring confidence in determining both the amplitude and the phase of the dominant mode.

The spatial resolution of the x-ray optical system itself was tested with the help of x-ray film as a detector and was found to be of order 6-7 μm (see Fig. 2). High throughput of the x-ray optical system allowed us to magnify the images by a factor of 20. However, the overall spatial resolution was still limited by the streak camera. In order to quantify the resolution of the x-ray crystal/streak camera system, a measurement of its modulation transfer function (MTF) was necessary. The MTF of the entire diagnostic system was obtained by imaging a knife-edge target. The derivative of the

measured edge profile gave the line-spread function (LSF) of the system, from which the MTF could be obtained by Fourier transform.[34] To reduce the noise introduced by differentiation, a non-linear least-squares fit was applied to the LSF. It was found that the LSF is well fitted by the sum of a Gaussian and a Lorentzian. The MTF was then obtained by applying Fourier transform to the resulting fit. For magnification of 20×, the MTF at l = 45 and 30 μm was found to be 0.6 and 0.4, respectively, and was used to correct the measured mode amplitude in the experiments.

The MTF was also verified directly by imaging undriven targets with known amplitudes (Fig. 3). The variation in measured amplitude (dashed lines) is due to the noise in our system. When averaged over longer time (solid lines), the measurements on targets of either wavelength are seen to reproduce the expected amplitudes. Amplitude of the noise gives us an idea of an experimental error (the width of the shaded area), with which we can measure the mass perturbations. In these and all of the following figures, the mode amplitude as a function of time was determined using a routine based on Fast Fourier analysis of the streaked images.

Since the spatial resolution of the system is limited by the spatial resolution of the streak camera, it is possible to improve the MTF of the whole system by increasing of the magnification of the X-ray optical system. Figure 4 shows a significant improvement in the image quality when the magnification was changed from 20 to 30. A 30× magnified image of a 400-lpi test mesh is shown on the left. The insert corresponds to the lower magnification of 20×. It is visibly more blurred than the image taken with higher magnification. The graph on the right side represents the MTFs measured for the two magnifications. The insert shows the lineouts of knife-edge images. The gray curve

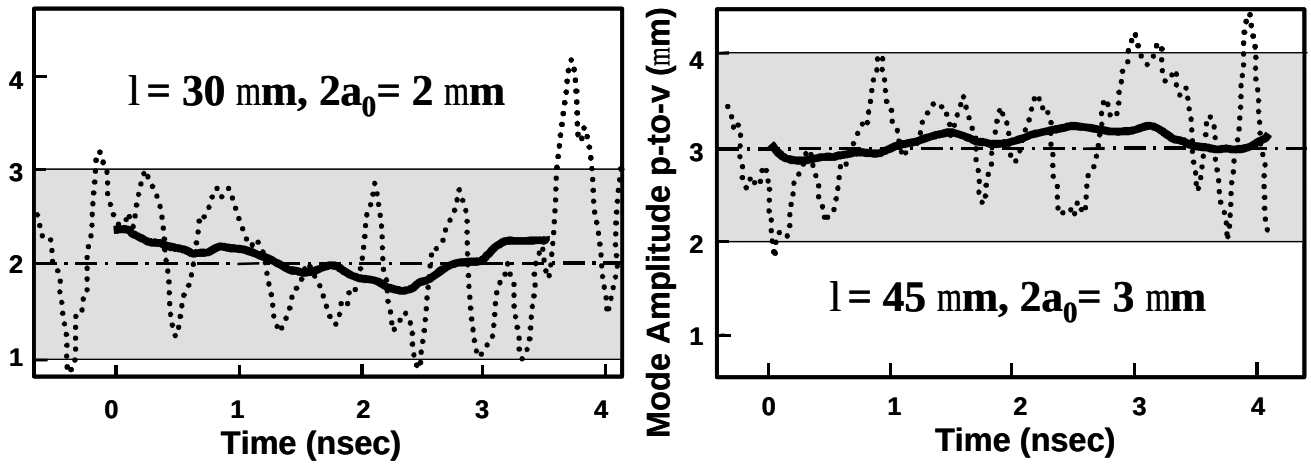

Fig. 3. Areal mass modulation as measured (dashed lines) and after smoothing by averaging over longer time (solid lines). Amplitude of the noise characterizes the experimental error bar for the areal mass modulation measurements (the width of the shaded area).

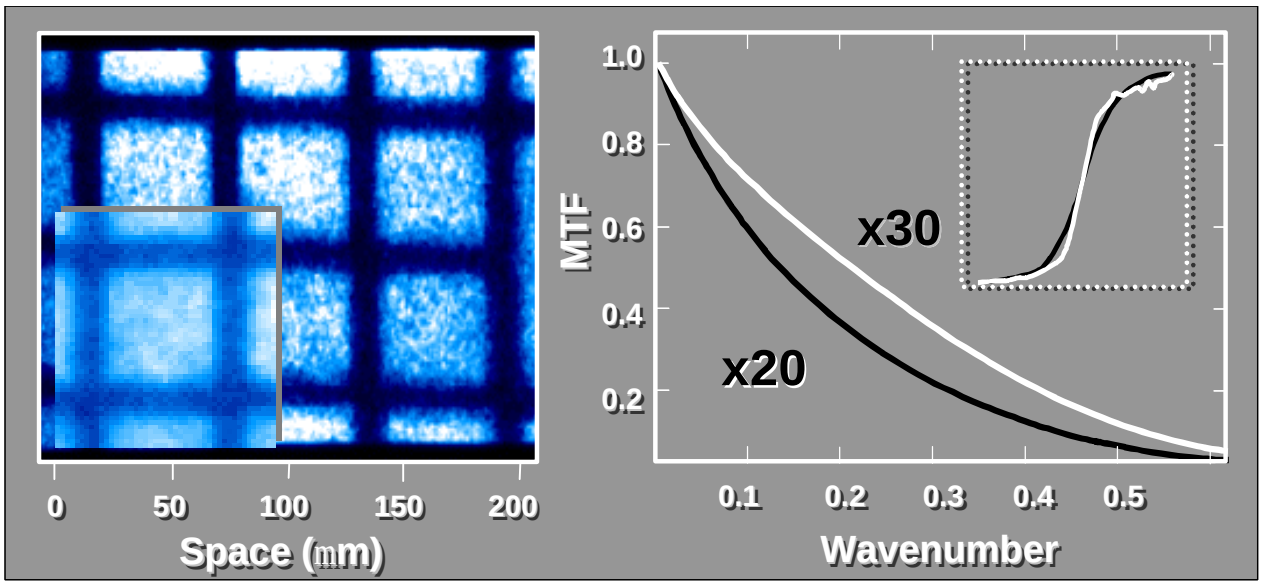

Fig. 4. Left: 30× magnified image of a 400-lpi test mesh (20× magnified image of the same in the insert.) Right: the MTFs measured for the two magnifications. The insert shows the lineouts of the two corresponding knife-edge images. The white curve corresponding to higher magnification is steeper than the black low-magnification one

corresponding to the higher magnification is steeper than the black low magnification one. Due to the decrease in the photon count we would be able to use the higher magnification only for targets with the thickness of 40 μm.

B. Experimental results: Ablative RM instability

For the experiments on ablative RM instability, we used planar plastic targets 40 to 99 μm thick, rippled on the front side as a 2-D sine wave $a_0 \sin kx$ with perturbation wavelength l = 30 or 45 μm. The streak records are Fourier transformed, giving both the amplitude and the phase of the dominant perturbation mode as functions of time. The observed modulation of the probing x-rays is exponentially related to mass modulation integrated over the line of sight, which is expressed in units of μm×g/cm^3. We present the MTF-corrected Fourier peak-to-valley areal mass modulation amplitudes normalized to the solid plastic density, 1.07 g/cm^3, thus expressing them in microns. Initially, the amplitude normalized this way simply equals the p-t-v amplitude of the front surface ripple. After the irradiation starts, however, the Fourier amplitude no longer can be interpreted simply as the amplitude of the interfacial ripples. Displacements of the rippled ablation front and of the rippled shock front launched into the target from its rippled surface, as well as the integrated density non-uniformity in the plasma between the shock and ablation fronts all contribute to the observed mass modulation. Theory and simulations[12-17] indicate that the contribution from the displacement of the ablation front becomes dominant long before the RT growth starts, see Fig.1 (a), but even then our normalized Fourier amplitude is not the same as the ripple amplitude, since the density at the ablation front is not the same as solid plastic density.

A clear example of the ablative RM oscillation is seen in Fig. 5, which shows the streak record (left), its lineouts at four different instants, and the Fourier amplitude of the dominant mode vs. time (right). The mass modulation amplitude grows almost by a factor of 5 within the first 1.5 ns, after which it starts decreasing. Substituting L = 65 μm, D = 4×10^6 cm/s into (6), we find that the rarefaction wave coming from the rear side breaks out at the front side, starting the RT growth, at about 2.4 ns (this estimate is consistent with our simulations). Figure 5 shows that the lateral mass flow in the *negative* direction (that is, decreasing the areal mass where it is high and increasing it where it is low) caused by the ablative RM oscillatory mechanism successfully competes against the RT growth (which would drive the mass laterally in opposite direction) for about $\Delta t_{RT} = 0.6$ ns, see (8). After the minimum of mass modulation is reached, at about half its first peak amplitude, the RT growth prevails, and the amplitude starts growing again, peaking at about 9 times the initial amplitude. At this time the laser pulse is over and the target decompresses.

For a thicker target, the rarefaction wave would break out later, hence the decreasing phase of the oscillations should last longer, leading eventually to the phase reversal of mass modulation.[12, 15] The target thickness L required to observe the phase reversal, all other conditions being the same as in Fig. 5, can be roughly estimated from (7), where the value of $r_D = 0.054$ appropriate for λ = 45 μm, should be used: L > 93 μm. In Fig. 6, we compare the time histories of the dominant mode amplitudes for two targets: one 65 μm thick (same curve as shown in Fig. 5), and the other 95 μm thick. The curve obtained for the thicker target is identical within the experimental error (the data is noisier because less light gets through the thicker target to the streak camera) to the time

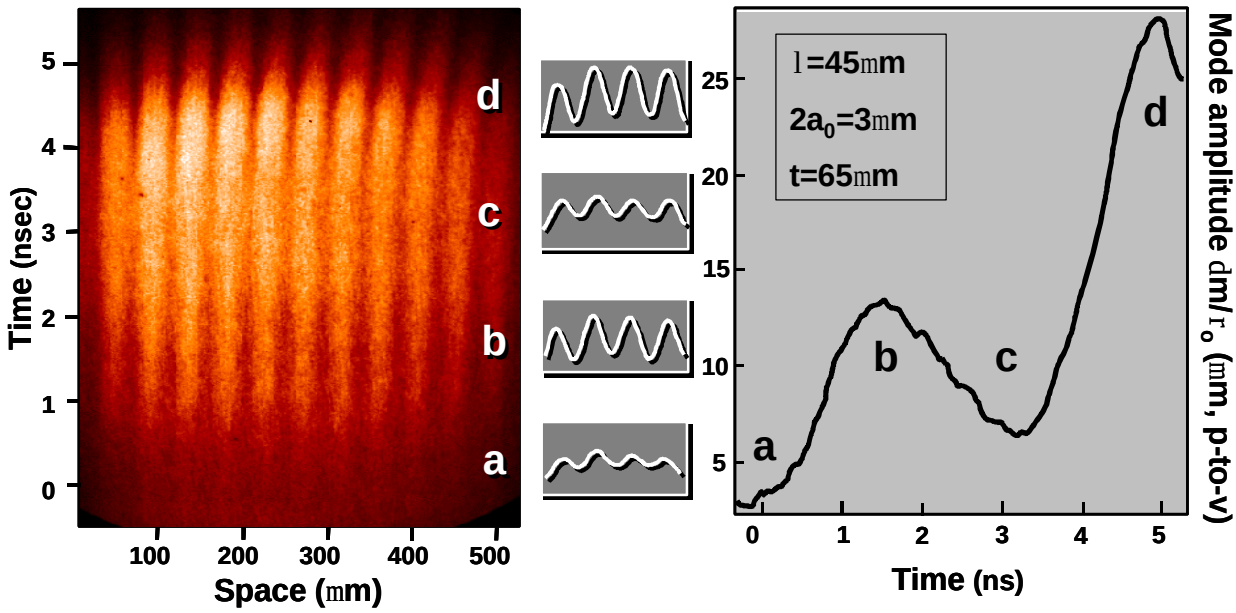

Fig. 5. Left: original streak record along with the amplitude lineouts taken across the ripples at four benchmarking times (the inserts). Right: the time-dependent Fourier amplitude of the dominant mode vs. time for a 65 μm thick target with λ = 45 μm and initial peak-to-valley amplitude $2a_0 = 3$ μm, also marked at four important times: beginning of the pulse, first peak, etc. The origin of time t = 0 here and elsewhere corresponds to the instant when the laser beam intensity reaches half maximum. The thickness of the shaded area approximately corresponds to the experimental uncertainty.

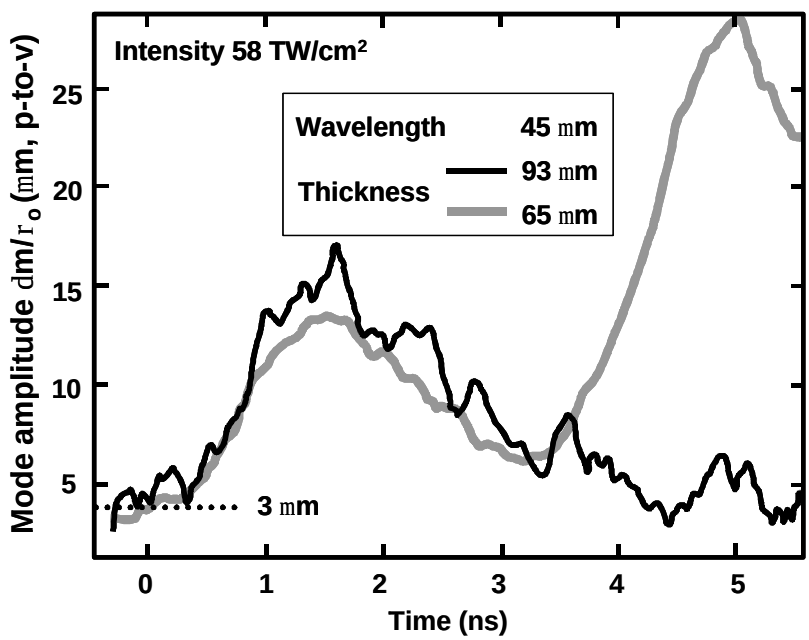

Fig. 6. Time histories of areal mass modulation amplitude compared for a 65 μm thick (gray line, same as in Fig. 5) and a 95 μm thick target (black line).

history recorded for a thinner target until the RT growth in the latter begins, as expected. For the thicker target, we find from (4): $t_{rb} = 3.6$ ns. Expecting about the same $\Delta t_{RT} \cong 6$ ns delay between the rarefaction breakout and the start of the observed RT growth as in Fig. 5, we conclude that the RT growth starting at about 4.3 ns could have been seen if the driving laser radiation was still on. Since it is already over at 4 ns, none of the RT growth is seen for the 95 μm thick target.

As illustrated by Eq. (2), the period of the ablative RM oscillations scales as $l r_D^{1/2}$, roughly as some positive power of λ. Therefore, to make the phase reversal of areal mass modulation observable, a shorter wavelength is needed. From Fig. 1(a) and Eqs. (5) and (7) one finds that for the shortest wavelength available to us, λ = 30 μm, the phase reversal is expected at about 3 ns, and the target thickness should be no less than 80 μm. Hence a 99 μm thick target should be thick enough to observe the phase reversal. This is indeed the case. Figure 7(a) compares the time histories for two targets, one 95 μm thick with the perturbation wavelength λ = 45 μm, $2a_0 = 3$ μm (same as in Fig. 6), and the other 99 μm thick with λ = 30 μm, $2a_0 = 2$ μm. The signal for the latter is noisier than for the former, due to both shorter wavelength and smaller initial amplitude. Figure 7(b) shows the measured real part of the amplitude and the phase of the dominant Fourier mode. The mass modulation amplitude is seen to pass through zero at about 3.3 ns, where a phase reversal is observed. After that, the perturbation amplitude starts to increase in the negative direction. Note that this is due to the oscillation continuing after the phase reversal rather than a beginning of the RT growth in the negative direction. Substituting λ = 30 μm, L = 99 μm and $D = 4\times10^6$ cm/s into (6) and (8), we obtain: $t_{rb} = 3.6$ ns,

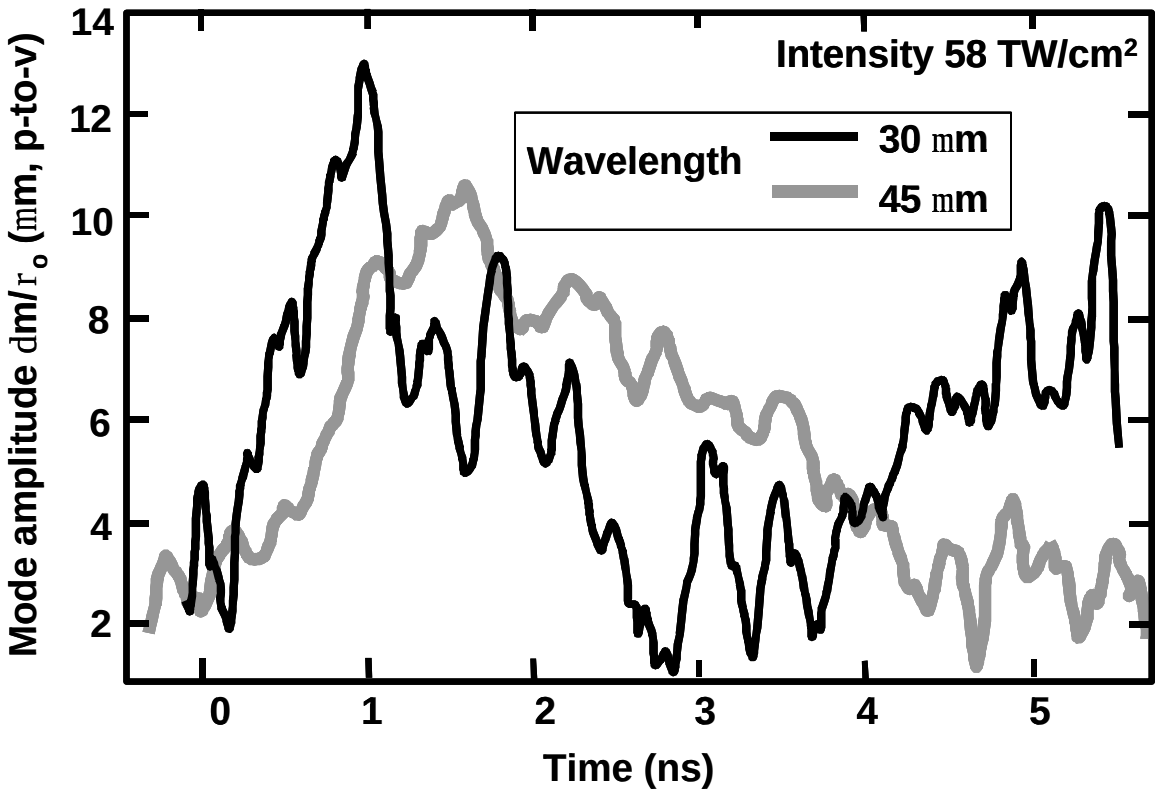

Fig. 7. (a) Time histories of areal mass modulation amplitudes compared for 95 μm thick target with λ = 45 μm (gray line) and 99 μm thick, λ = 30 μm target (black line). Initial amplitudes are normalized to 2 μm peak-to-valley.

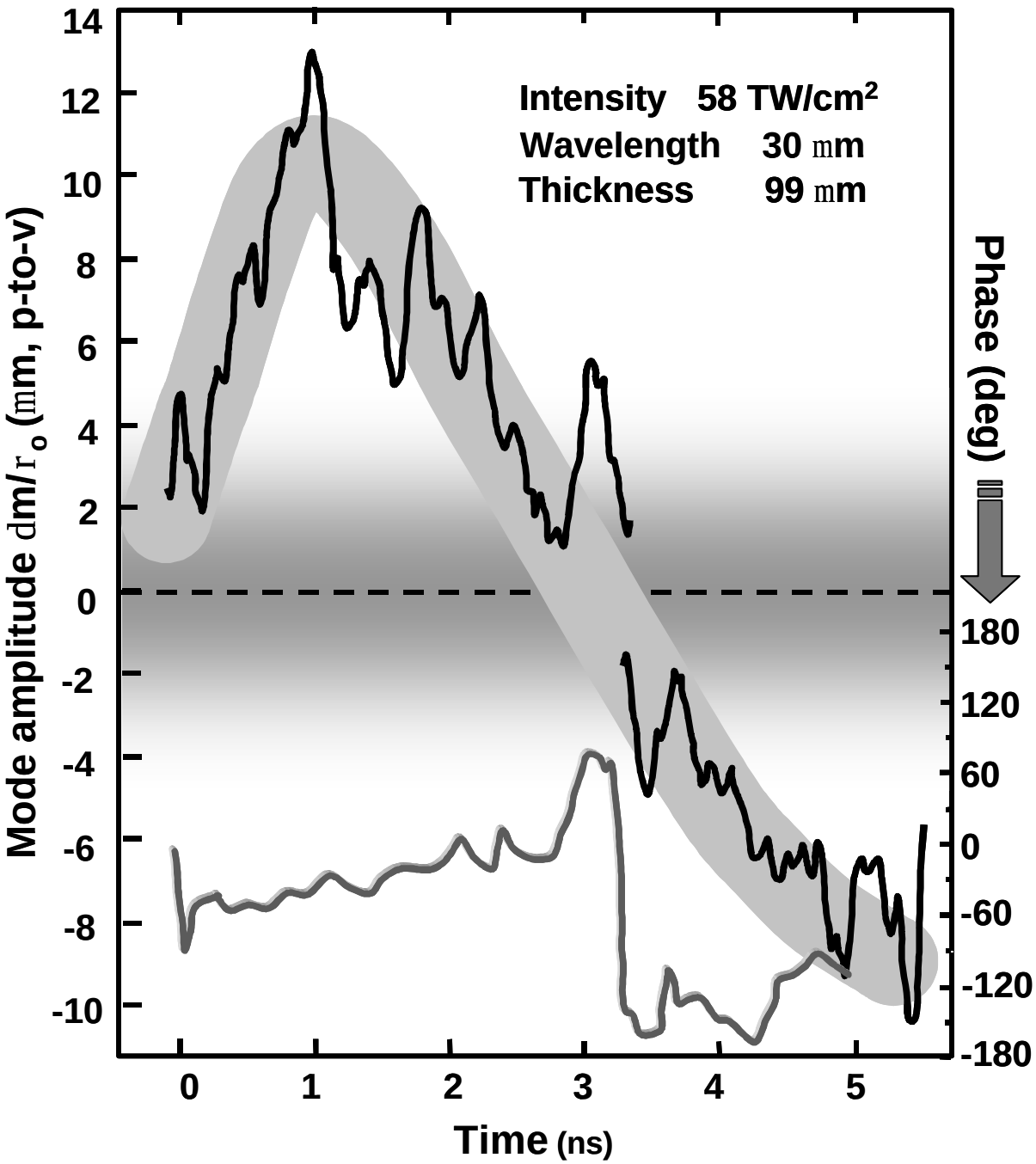

Figure 7(b). The real part of the amplitude and phase of mass modulation vs. time for the target with λ = 30 μm. The thickness of the shaded areas approximately corresponds to the experimental uncertainty.

$\Delta t_{RT} = 0.6$ ns, so that the phase reversal occurs before the onset of the exponential RT growth. Indeed, as discussed above, no such growth is observed (and no phase reversal is seen) in a target of almost the same thickness L = 95 μm with a longer perturbation wavelength, l = 45 μm. This is consistent with the analytical theory, which for the latter case predicts no phase reversal before 3.75 ns, which is actually after the rarefaction breakout. It is instructive to contrast Fig. 7(a) to Fig. 8 below, where a similar comparison is made for thinner targets, and the RT growth is seen to start at the same time for both perturbation wavelengths. As pointed out in Section II, the observed phase reversal is a clear indication that the oscillation of areal mass amplitude is caused by the ablative RM instability rather than the rippled shock front.

In Figure 8, we compare the RM oscillations in two targets of the same thickness, 65 μm (same as in Fig. 5; thinner than in Fig. 7): one with l = 45 μm, $2a_0 = 3$ μm and the other with l = 30 μm, $2a_0 = 2$ μm. In the figure, both curves are normalized to the same initial amplitude, 1 μm. The two curves are qualitatively similar, demonstrating reproducibility and robustness of the oscillatory behavior under varied conditions. The mass modulation amplitude in both cases reaches a peak and then decreases until the RT growth starts shortly after 3 ns in both cases, as expected ($t_{rb} \cong 2.4$ ns for both targets, $\Delta t_{RT} = 0.5$ ns and 0.6 ns for short and long wavelength, respectively). The first peaks in both cases are observed at about the same time, which is not in contradiction to the theory.[15, 16] Taking into account that the period of oscillations of the ablation front scales as $l r_D^{1/2}$, whereas the period of shock-induced oscillations scales as l [cf. Eqs. (2) and (4), respectively], and comparing Fig. 1(a) with a similar graph plotted for l = 45 μm, we

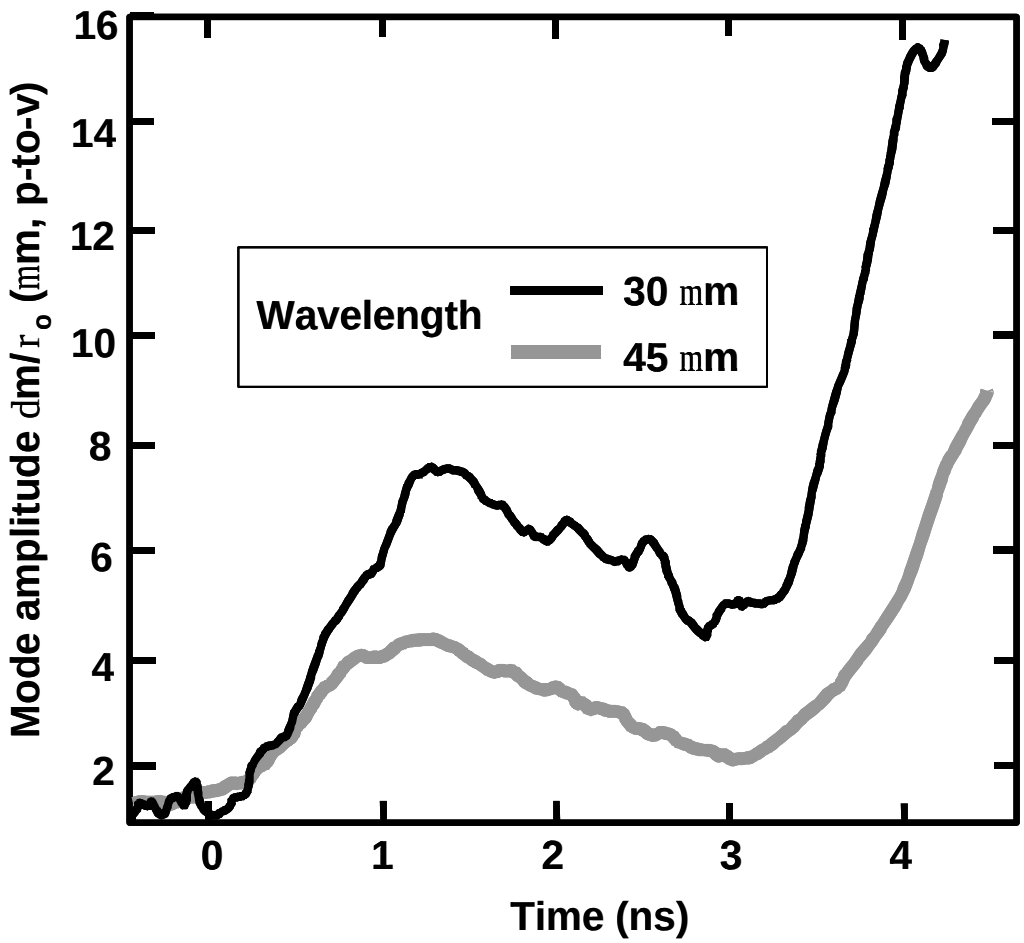

Fig. 8. Time histories of areal mass modulation amplitudes compared for 65 μm thick targets with l = 45 μm (gray line, same as in Fig. 5) and l = 30 μm (black line). Initial amplitudes are normalized to 1 μm peak-to-valley.

find that the first peak of mass modulation amplitude for the l = 45 μm case occurs about 0.4 ns later than for the l = 30 μm case - a difference that is hardly resolvable at our level of accuracy. An unexpected well-resolved feature is the large absolute difference between the two normalized curves in Fig. 7. The theory, [15, 16] as well as our simulations, see below, predict them to be much closer to each other.

Our experimental results are compared to simulations performed in two dimensions (2D) using the FAST2D hydrocode developed at the Naval Research Laboratory[35] (more details about the code and further references are given in Refs. 12, 16, 18). Figure 9 presents a comparison similar to that shown in Fig. 6: same perturbation wavelength, different thickness of the two targets. There is a qualitative agreement with Fig. 6: for a thinner target, the RT growth starts earlier, while for a thicker target the oscillation cycle continues. We see also some difference: in a 94 μm thick target, the simulated amplitude reaches a minimum and features the onset of the RT growth shortly before the laser pulse is over at 4 ns. It appears that in the simulation the RT growth starts slightly earlier and proceeds somewhat faster than seen in our experiment. The same conclusion could be drawn from Fig. 10, where evolution of perturbations with different wavelengths in targets of the same thickness are compared (cf. Fig. 8). Note that the amplitudes of the first peaks for l = 30 μm and 45 μm in the experiment differ considerably, whereas in the simulation they are quite close to each other, in agreement with the theory.

C. Experimental results: Feedout

For the experiments on feedout, we used planar plastic targets 40 to 60 μm thick, rippled at the rear side with perturbation wavelength λ = 30 or 45 μm. For our

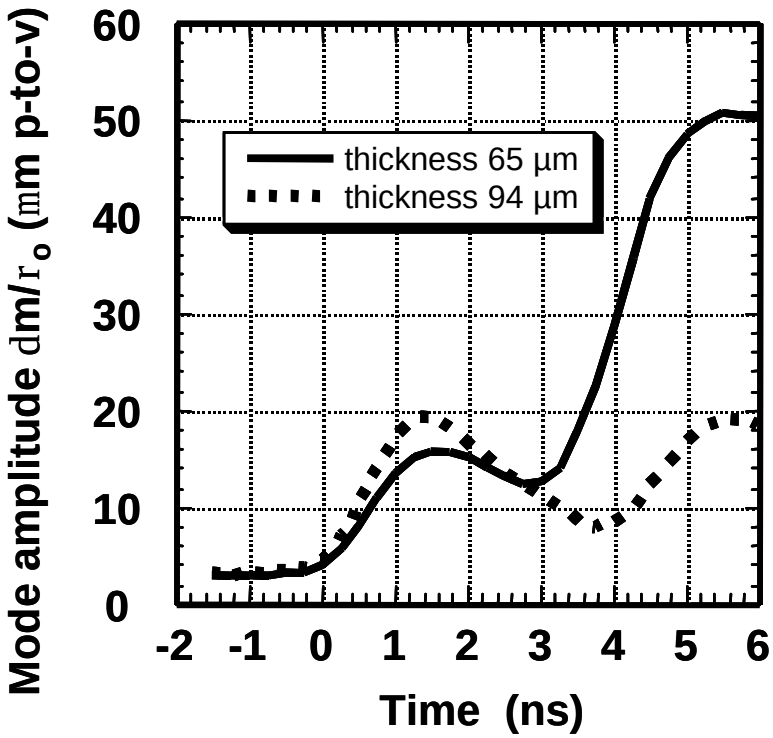

Fig. 9. Simulated time histories of areal mass modulation amplitude compared for a 65 µm thick (dotted line) and a 94 µm thick target (solid line) with λ = 45 µm.

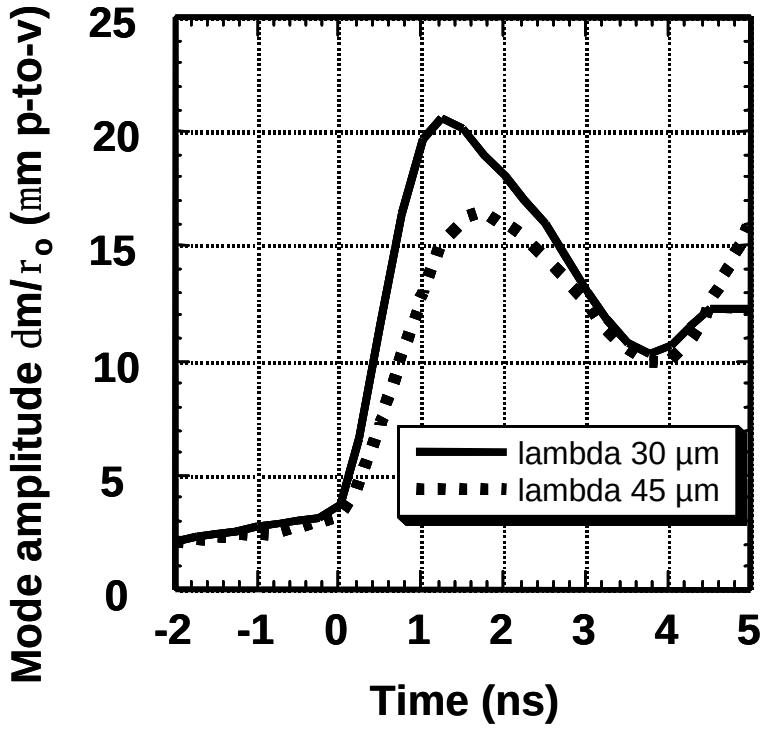

Fig. 10. Simulated time histories of areal mass modulation amplitude compared for 65 µm thick targets with λ = 30 µm and 45 µm.

experimental conditions, the theory[18] and simulations predict two phase reversals of mass modulation. Observing the feedout-related oscillations is even more challenging than those caused by the ablative RM instability. Indeed, the latter occur at larger perturbation amplitudes, typically exceeding its initial value by a factor of 3 to 5 (as in Figs. 5-8). Here, on the other hand, we have to measure mass perturbations smaller than the initial amplitude. It was still possible thanks to the high resolution and contrast of our diagnostics.

Figure 11 shows an original streak record of a target with thickness 60 μm, l = 46 μm. Also shown are its lineouts at three different times. The two phase reversals illustrated by the lineouts are clearly visible on the original streak record. The light and dark stripes that correspond to low and high areal mass, respectively, are seen at early time, and then disappear, as if they were smeared out in a horizontal band ~0.5 ns wide. Then the stripes reappear, but the light and dark ones are interchanged, indicating the first 180° phase reversal. It occurs about the time found from Eqs. (9) and (11) [or, more accurately, from Eq. (1) of Ref. 22], $t \cong 2$ ns.

For a much thicker target, the theory[18] predicts the second phase reversal to occur due to the areal mass oscillations in a rippled rarefaction wave, see Fig. 1(b). All other conditions being equal, we would need a ~200 μm thick target driven by a >5 ns long laser pulse to observe it at $t \cong 4.8$ ns, both of which exceed the capabilities of our experiment. In our case, shortly after the first phase reversal, at about 2.5 ns, the rippled rarefaction wave breaks out at the front surface of the target, and the RT growth in the positive direction (at the initial phase) starts from there, as explained in Section II. This causes the phase of areal mass modulation to be reversed again, this time at about 4 ns,

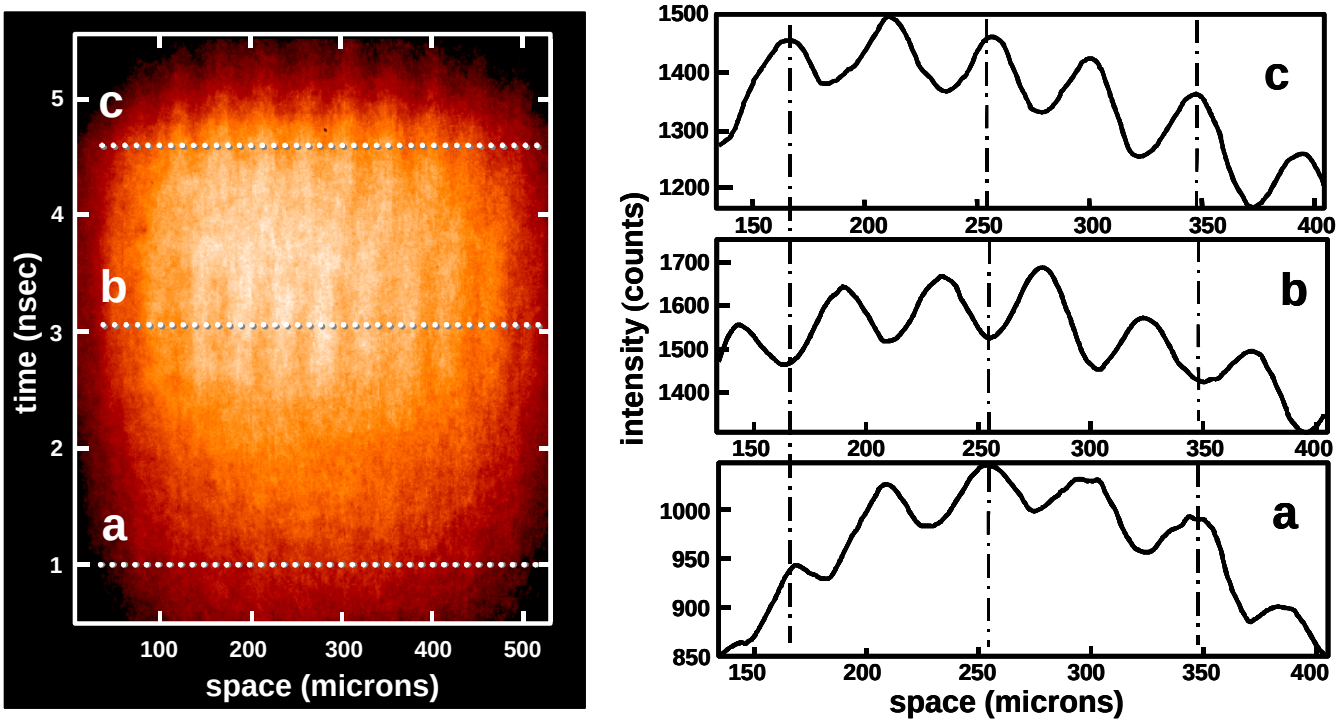

Fig. 11. Left: original streak record for a feedout target. Right: its lineouts at three different times for target thickness 60 μm and l = 46 μm.

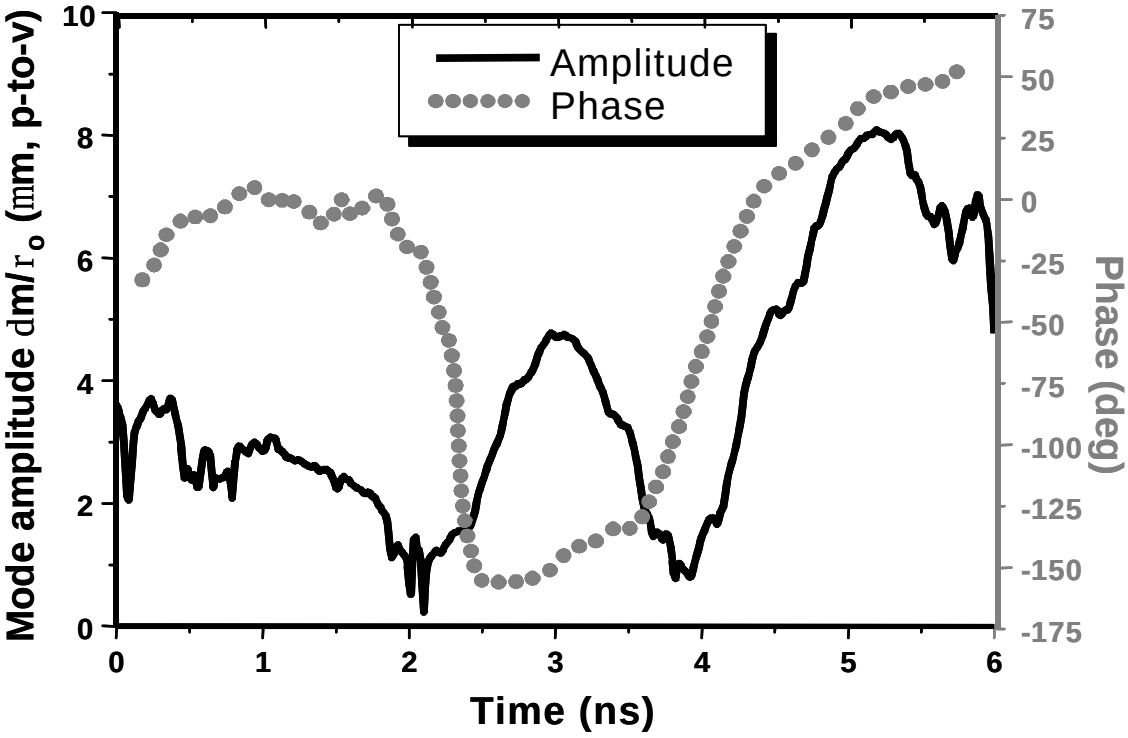

Fig. 12. Time histories of areal mass modulation amplitude and phase for the streak record shown in Fig. 11.

producing another smeared band on the original streak record. The subsequent RT growth is also clearly seen: the dark and light stripes, representing peaks and valleys of areal mass distribution, respectively, become more pronounced at late times.

Figure 12 shows the amplitude and phase of mass modulation vs. time for the same case. Two rapid changes of phase are seen at about 2 and 4 ns, confirming visual observation of two phase reversals on the original streak record in Fig. 11.

Figure 13 compares the evolution of mass modulation for two targets of different thickness: 60 μm and 40 μm. As expected, during the time that the evolution is governed by the mass variation in a rippled rarefaction wave, there is little difference between the two time histories: both feature the first phase reversal after ~0.5 ns after the shock breakout, at ~2 and ~1.5 ns, respectively. In a thinner target, however, the reflected rarefaction wave breaks out earlier, at about 1.5 ns, Then, as described in Section II [see Fig. 1(b)], the lateral mass flow in the rippled rarefaction wave increases the amplitude in the *negative* direction, but the RT growth, starting from the initially planar front surface, increases it in the positive direction. At about 2 ns, the fast RT growth prevails, and the absolute value of the modulation amplitude starts decreasing after having reached a negative peak less than the initial amplitude. Shortly after this, it reverses its phase again, and keeps growing. This can be compared to a 60 μm target, where the rippled rarefaction wave has more time to build up the negative peak. Here, the RT growth prevails at about 3 ns, the negative peak reaching twice the initial amplitude. Then we see qualitatively the same evolution as observed for a 40 μm target: decrease, phase reversal, and the subsequent RT growth.

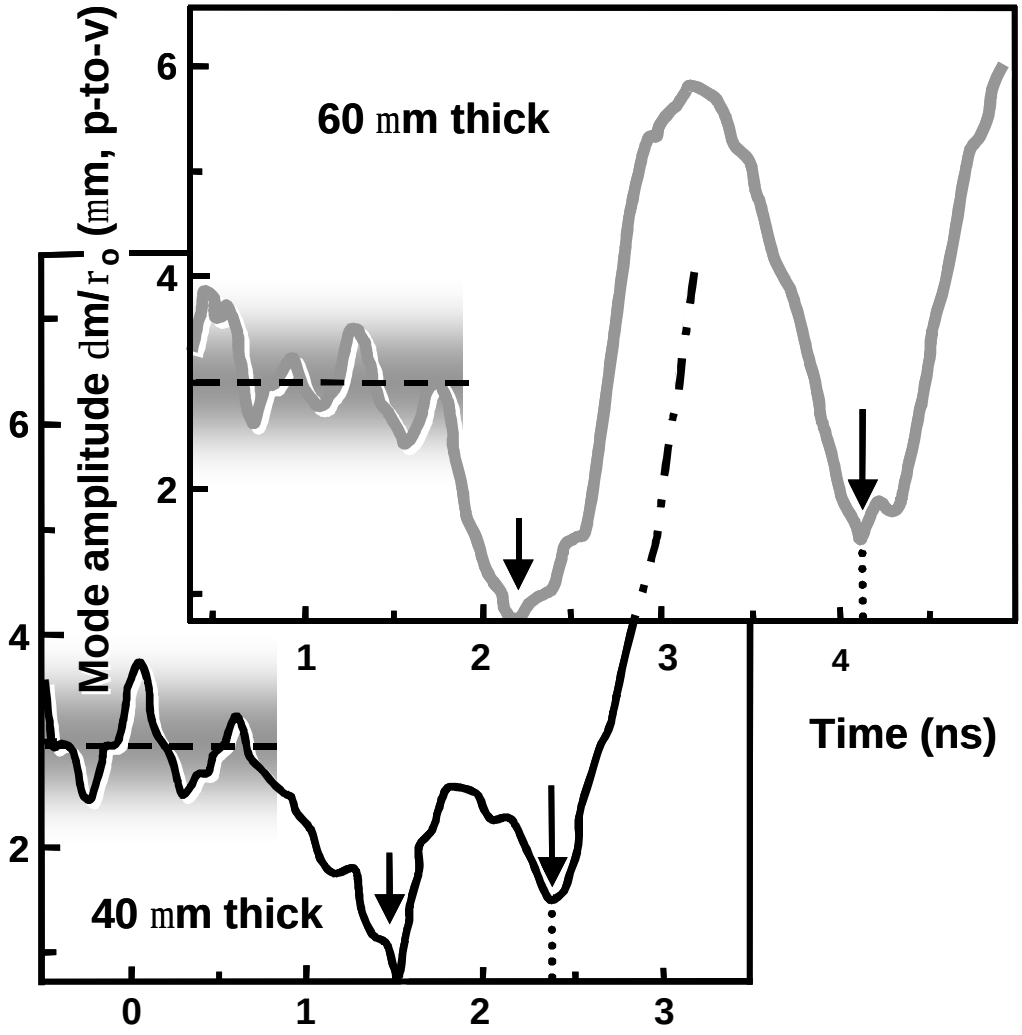

Fig. 13.

Fig. 13. Time histories of areal mass modulation amplitudes compared for a 60 μm thick (top, same as in Figs. 9 and 10) and a 40 μm thick target (bottom). Arrows indicate the phase reversals. The thickness of the shaded areas approximately corresponds to the experimental uncertainty.

The period of oscillations in a rippled rarefaction wave scales proportionally to the perturbation wavelength.[18] Therefore, the evolution of mass modulation in two targets of the same thickness with different perturbation wavelengths is expected to differ qualitatively from that shown in Fig. 8. Between the shock breakout at the rear surface and the reflected rarefaction breakout at the front surface (this time interval is the same for both targets), the short-wavelength perturbation goes deeper into the negative peak. Then, when the time comes for the RT growth in the positive direction (cf. Fig. 13), the short-wavelength perturbation amplitude, having reached farther into the negative, finds itself lagging behind. The long-wavelength perturbation, having started its RT growth from a smaller negative amplitude, reaches higher positive values. This is indeed confirmed by Fig. 14, where two 60 μm thick targets with rippled rear surfaces are compared, one with l = 45 μm, and another with l = 30 μm. In Fig. 14, the mass modulation amplitude is plotted with a proper sign: negative between the two phase reversals. We see that, in contrast with Fig. 8, within the time frame of the Nike laser pulse, the long-wavelength modulation grows to higher amplitude than the short-wavelength one.

The trends seen in the feedout experiments are compared to the simulation results in Figs. 15 and 16. Figure 15 presents a comparison similar to that shown in Fig. 13: same wavelength, different thickness of the two targets. As expected, in the thicker target the growth of the modulation amplitude in the negative direction proceeds farther, and the corresponding minimum is deeper. It is not as deep, however, as observed (cf. Fig. 14), which is about twice the initial amplitude. As in Section III.B (e. g., cf. Figs. 6, 9), it appears that the RT growth that competes with the downward trend, eventually making

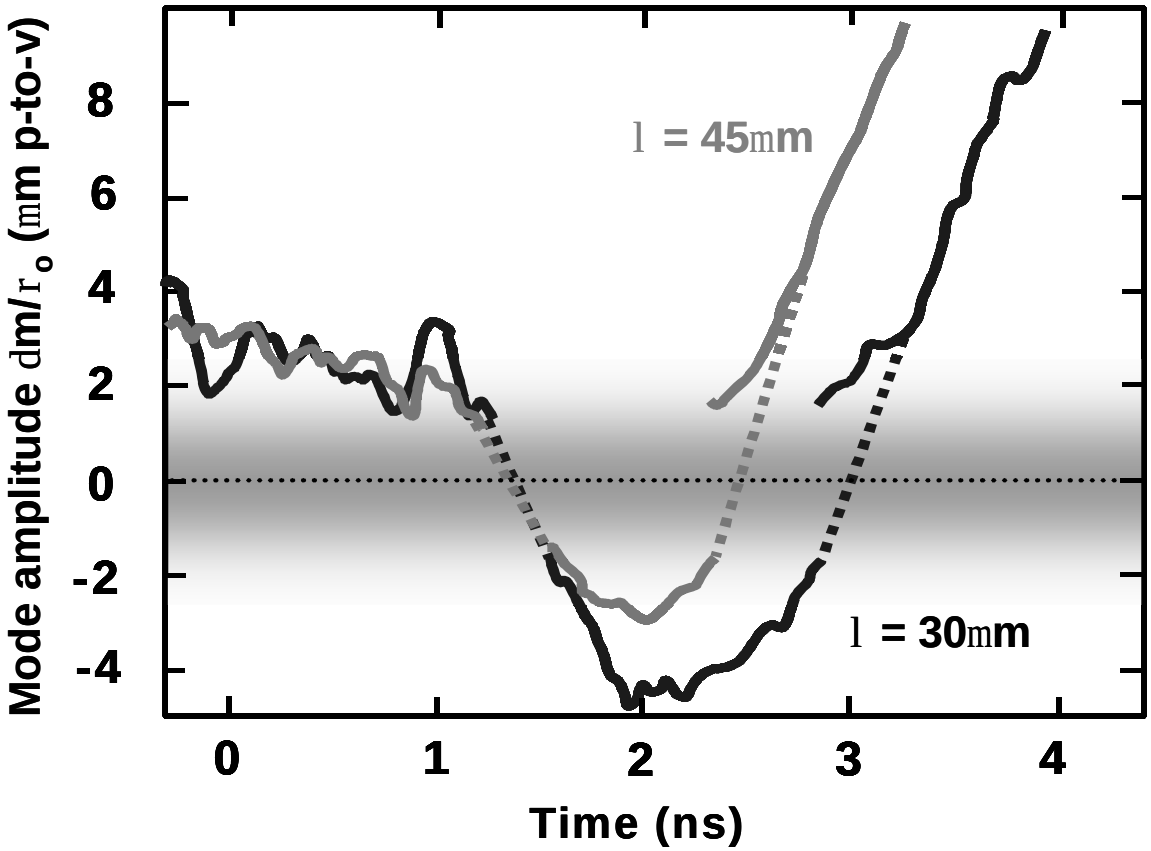

Fig. 14. Time histories of areal mass modulation amplitudes compared for 60 μm thick targets with l = 45 μm (gray line) and l = 30 μm (black line). In the gray area around zero, the measured amplitudes are in the noise. Initial amplitudes are normalized to 3 μm peak-to-valley. The thickness of the shaded area approximately corresponds to the experimental uncertainty.

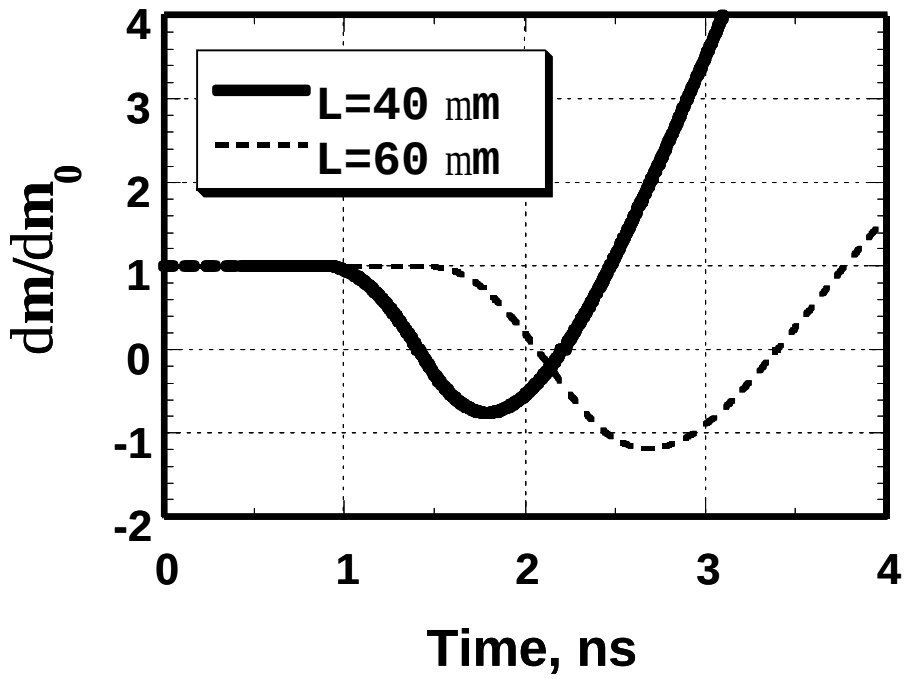

Fig. 15. Simulated time histories of areal mass modulation amplitude compared for 60 μm thick (dashed line) and 40 μm thick targets (solid line) with λ = 45 μm.

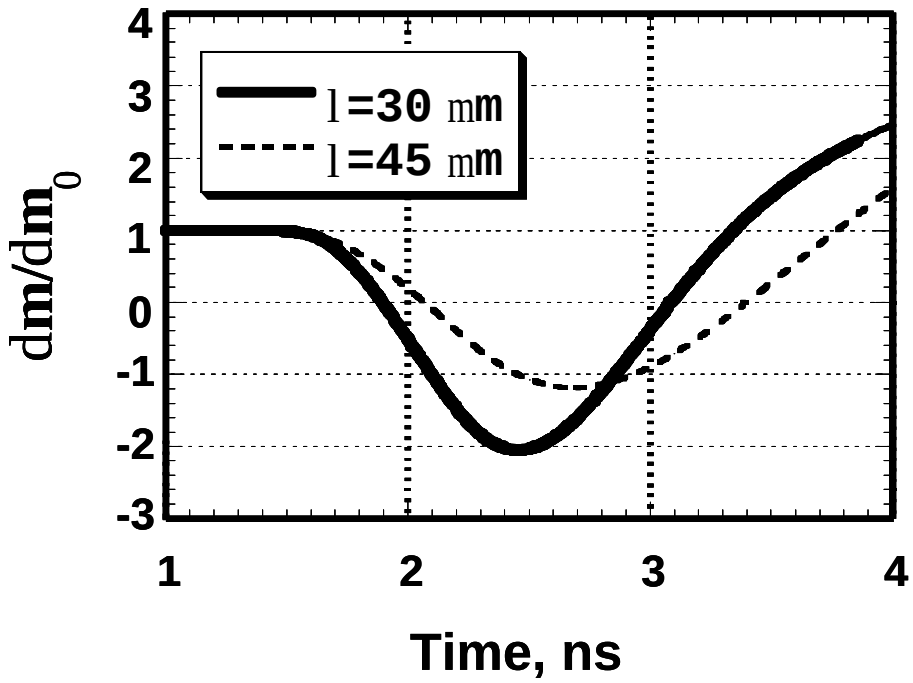

Fig. 16. Simulated time histories of areal mass modulation amplitude compared for 60 μm thick targets with λ = 45 μm (dashed line) and λ = 30 μm (solid line).

the mass modulation amplitude increase in the positive direction, starts somewhat earlier in the simulation than in the experiment, thus producing a shallower negative peak. The same is indicated by Fig. 16, where the oscillations are compared for two targets of the same thickness that have different perturbation wavelengths. Indeed, the oscillation proceeds faster for the target with a shorter wavelength, l = 30 μm, where a deeper negative peak is developed. However, once the fast RT growth in the positive direction starts, it also proceeds faster at a shorter wavelength. In the simulation, there is enough time to reach a higher positive amplitude in the target with l = 30 μm compared to the target with l = 45 μm, in contrast with what is seen in Fig. 14. Once again, the RT growth in the experiment seems to start later.

IV. Conclusions

In our experiments we have observed an oscillatory evolution of areal mass perturbations in an ablatively driven target during the shock-rarefaction transit time. Though these observations were made in a planar geometry, they are nevertheless relevant to understanding and modeling the RT instability seeding in spherical targets. The front surface ripple, which excites the ablative RM instability, corresponds to a mode of the outer surface roughness of a spherical direct-drive target. Both theory and simulations[12-17] indicate that the physics of RM oscillations excited by either surface ripple or single-mode, constant phase laser beam non-uniformity, is identical. Using the former case to validate the codes, the capacity for modeling the latter can be improved. Similarly, the rear surface ripple corresponds to a mode of the inner surface roughness of a spherical target, which seeds the RT growth via the feedout mechanism, regardless of whether a direct or indirect drive is used.

Prior to our experiments, theory and simulations predicted the oscillations of areal mass to occur during the shock-rarefaction transit time. Our experimental results are in a general agreement with these predictions. Qualitatively, the agreement is fine: the sequence of phases when the mass modulation amplitude increases and decreases, the number of its phase reversals, the changes in the evolution expected when either the target thickness or the perturbation wavelength is varied, are all in accord with the theory. Quantitatively, the agreement is reasonable; in particular, the periods and amplitudes of the oscillations, the positions of the positive and negative peaks are typically close to the observed values. In one respect, however, there is a consistent quantitative discrepancy between our experimental results and the 2-D computer simulations. For both front and rear surface ripples, the simulations have in all cases predicted the RT growth to start slightly earlier than observed (by about 0.4 ns) and to proceed somewhat faster. It could be due to some factors that might affect the early-time evolution, but have not been accounted for in our simulations: i. e., any low-intensity amplified spontaneous emission (ASE) incident on the target for tens of ns prior to the main pulse. This issue has to be resolved in our future studies.

Numerous attractive opportunities are open for new experiments on the oscillatory early-time behavior that could be made using our diagnostics. For instance, as suggested in Ref. 12, the shock transit time can be extended without increasing the areal mass of the target (and thereby decreasing the photon count). To do this, we need low-density foam targets (either rippled or with a solid rippled cover on top) instead of solid plastic targets. Using deuterium-wicked foams, [33] it might even be possible to observe the ablative RM oscillations in a liquid deuterium target. Deuterium is transparent for the backlighting

keV x-ray radiation, but the density variation in the background plastic foam should be observable with our diagnostics. For the feedout geometry, it is interesting to test the theoretical predictions that in some situations there should be one, three, or even four phase reversals rather than two that we have observed. Three or one phase reversals are expected when the main laser pulse is preceded by a substantial "foot"; four are possible when the ratio of the target thickness to the perturbation wavelength is above ~4. If the number of phase reversals were odd, then the RT bubbles would be produced, counter-intuitively, where the target was initially thicker.[18]

Acknowledgments

The authors wish to thank the Nike Laser Crew for their excellent technical support and J. L. Weaver, J. W. Bates (NRL) and Y. Chan (SAIC) for their important contributions. Fruitful consultations with A. Y. Faenov and T. A. Pikuz of VNIIFTRI, Moscow, are gratefully acknowledged.

This work was supported by the U.S. Department of Energy, Defense Programs.

References

[1] J. D. Lindl, Phys. Plasmas **2**, 3933 (1995); *Inertial Confinement Fusion: The Quest for Ignition and Energy Gain Using Indirect Drive* (Springer, Heidelberg, 1997).

[2] S. E. Bodner, D. G. Colombant, J. H. Gardner, R. H. Lehmberg, S. P. Obenschain, L. Phillips, A. J. Schmitt, J. D. Sethian, R. L. McCrory, W. Seka, C. P. Verdon, J. P. Knauer, B. B. Afeyan, H. T. Powell, Phys. Plasmas **5**, 1901 (1998).

[3] T. R. Dittrich, S. W. Haan, M. M. Marinak, S. M. Pollaine, D. E. Hinkel, D. H. Munro, C. P. Verdon, G. L. Strobel, R. McEachern, R. C. Cook, and C. C. Roberts D. C. Wilson, P. A. Bradley, L. R. Foreman, and W. S. Varnum, Phys. Plasmas **6**, 2164 (1999); T. R. Dittrich, S. W. Haan, M. M. Marinak, S. M. Pollaine, and R. McEachern, Phys. Plasmas **5**, 3708 (1998).

[4] P. W. McKenty, V. N. Goncharov, R. P. J. Town, S. Skupsky, R. Betti, and R. L. McCrory, Phys. Plasmas **8**, 2315 (2001); S. E. Bodner, D. G. Colombant, A. J. Schmitt, M. Klapisch, Phys. Plasmas **7**, 2298 (2000); L. Phillips, J. H. Gardner, S. E. Bodner, D. Colombant, S. P. Obenschain, A. J. Schmitt, J. P. Dahlburg, T. K. Lehecka, M. Klapisch, A. Bar-Shalom, Laser and Particle Beams **17**, 225 (1999); D. Campbell and W. J. Hogan, Plasma Phys. Control. Fusion **41**, B39 (1999).

[5] S. E. Bodner, Phys. Today **54**, 12 (2001); J. Dawson, Phys. Today **54**, 21 (2001).

[6] J. Grun, M. H. Emery, S. Kacenjar, C. B. Opal, E. A. McLean, S. P. Obenschain, B. H. Ripin, and A. Schmitt, Phys. Rev. Lett. **53**, 1352 (1984); J. Grun, M. E. Emery, C. K. Manka, T. N. Lee, E. A. McLean, A. Mostovych, J. Stamper, S. Bodner, S. P. Obenschain, and B. H. Ripin, Phys. Rev. Lett. **58**, 2672 (1987); C. J. Pawley, S. E.

Bodner, J. P. Dahlburg, S. P. Obenschain, A. J. Schmitt, J. D. Sethian, C. A. Sullivan, J. H. Gardner, Y. Aglitskiy, Y. Chan, and T. Lehecka, Phys. Plasmas **6**, 565 (1999).

[7] M. Desselberger, O. Willi, M. Savage, and M. J. Lamb, Phys. Rev. Lett. **65**, 2997 (1990); M. Desselberger and O. Willi, Phys. Fluids B **5**, 896 (1993).

[8] H. Azechi, M. Nakai, K. Shigemori, N. Miyanaga, H. Shiraga, H. Nishimura, M. Honda, R. Ishizaki, J. G. Wouchuk, H. Takabe, K. Nishihara, K. Mima, A. Nishiguchi A, and T. Endo, Phys. Plasmas **4**, 4079 (1997); K. Shigemori, H. Azechi, M. Honda, K. Meguro, N. Miyanaga, H. Takabe, and K. Mima, Phys. Rev. Lett. **78**, 250 (1997).

[9] B. A. Remington, S. W. Haan, S. G. Glendinning, J. D. Kilkenny, D. H. Munro, and R. J. Wallace, Phys. Fluids B **4**, 967 (1992); B. A. Remington, S. V. Weber, M. M. Marinak, S. W. Haan, J. D. Kilkenny, R. J. Wallace, and G. Dimonte, Phys. Rev. Lett. **73**, 545 (1994); Phys. Plasmas **2**, 241 (1995).

[10] J. P. Knauer, R. Betti, D. K. Bradley, T. R. Boehly, T. J. B. Collins, V. N. Goncharov, P. W. McKenty, D. D. Meyerhofer, V. A. Smalyuk, C. P. Verdon, S. G. Glendinning, D. H. Kalantar, and R. G. Watt, Phys. Plasmas **7**, 338 (2000).

[11] M. H. Emery, J. H. Gardner, R. H. Lehmberg, and S. P. Obenschain, Phys. Fluids B **3**, 2640 (1991).

[12] A. L. Velikovich, J. P. Dahlburg, J. H. Gardner, and R. J. Taylor, Phys. Plasmas **5**, 1491 (1998).

[13] A. L. Velikovich, J. P. Dahlburg, A. J. Schmitt, J. P. Gardner, L. Phillips, F. L. Cochran, Y. P. Chong, G. Dimonte, and N. Metzler, Phys. Plasmas **7**, 1662 (2000);

[14] R. Ishizaki and K. Nishihara, Phys. Rev. Lett. **78**, 1920 (1997); Phys. Rev. E **58**, 3744 (1998); N. Matsui, K. Mima, M. Honda, and A. Nishiguchi, J. Plasma Phys. **61**, 43 (1999).

[15] V. N. Goncharov, Phys. Rev. Lett. **82**, 2091 (1999).

[16] N. Metzler, A. L. Velikovich, and J. P. Gardner, Phys. Plasmas **6**, 3283 (1999); A. J. Schmitt, A. L. Velikovich, J. H. Gardner, C. Pawley, S. P. Obenschain, Y. Aglitskiy, and Y. Chan, Phys. Plasmas **8**, 2287 (2001).

[17] V. N. Goncharov, S. Skupsky, T. R. Boehly, J. P. Knauer, P. McKenty, V. A. Smalyuk, R. P. J. Town, O. V. Gotchev, R. Betti, and D. D. Meyerhofer, Phys. Plasmas **7**, 2062 (2000);

[18] A. L. Velikovich, A. J. Schmitt, J. H. Gardner and N. Metzler, Phys. Plasmas **8**, 592 (2001).

[19] J. Sanz, Phys. Rev. Lett. **73**, 2700 (1994); A. R. Piriz, J. Sanz, and L. F. Ibañez, Phys. Plasmas **4**, 1117 (1997); A. R. Piriz, Phys. Plasmas **8**, 997 (2001).

[20] Y. Aglitskiy, T. Lehecka, S. Obenschain, S. Bodner, C. Pawley, K. Gerber, J. Sethian, C. M. Brown, J. Seely, U. Feldman, G. Holland, Applied Optics - OT **37**, 5253 (1998); Y. Aglitskiy, T. Lehecka, S. Obenschain, C. Pawley, C. M. Brown and J.Seely, Rev. Sci. Instrum. **70**, 530 (1999).

[21] Y. Aglitskiy, A. L. Velikovich, M. Karasik, V. Serlin, C. J. Pawley, A. J. Schmitt, S. P. Obenschain, A. N. Mostovych, J. H. Gardner, and N. Metzler, Phys. Rev. Lett. **87**, 265001 (2001).

[22] Y. Aglitskiy, A. L. Velikovich, M. Karasik, V. Serlin, C. J. Pawley, A. J. Schmitt, S. P. Obenschain, A. N. Mostovych, J. H. Gardner, and N. Metzler, Phys. Rev. Lett. **87**, 265002 (2001).

[23] V. N. Goncharov, R. Betti, R. L. McCrory, P. Sorotokin, C. P. Verdon, Phys. Plasmas **3**, 1402 (1996); R. Betti, V. N. Goncharov, R. L. McCrory, C. P. Verdon, Phys. Plasmas **5**, 1446 (1998).

[24] S. E. Bodner, Phys. Rev. Lett. **33**, 761 (1974).

[25] Ya. B. Zel'dovich and Yu. P. Raizer, *Physics of Shock Waves and High-Temperature Hydrodynamic Phenomena* (Academic Press, New York, 1966), Vol. 2.

[26] T. Endo, K. Shigemori, H. Azechi, A. Nishiguchi, K. Mima. M. Sato, M. Nakai, S. Nakaji, N. Miyanaga, S. Matsuoka, A. Ando, K. A. Tanaka, and S. Nakai, Phys. Rev. Lett. **74**, 3608 (1995).

[27] K. Shigemori, M. Nakai, H. Azechi, K. Nishihara, R. Ishizaki, T. Nagaya, H. Nagatomo, and K. Mima, Phys. Rev. Lett. **84**, 5331 (2000).

[28] R. Betti, V. Lobatchev, and R. L. McCrory, Phys. Rev. Lett. **81**, 5560 (1998).

[29] D. P. Smitherman, R. E. Chrien, N. M. Hoffman, and G. R. Magelssen, Phys. Plasmas **6**, 932 (1999).

[30] S. P. Obenschain, S. E. Bodner, D. Colombant, K. Gerber, R. H. Lehmberg, E. A. McLean, A. N. Mostovych, M. S. Pronko, C. J. Pawley, A. J. Schmitt, J. D. Sethian, V. Serlin, J. A. Stamper, C. A. Sullivan, J. P. Dahlburg, J. H. Gardner, Y. Chan, A. V. Deniz, J. Hardgrove, T. Lehecka, M. Klapisch, Phys. Plasmas **3**, 2098 (1996).

[31] A. V. Rode, A. M. Maksimchuk, G. V. Sklizkov, A. Ridgley, C. Danson, N. Rizvi, R. Bann, E. Forster and I. Uschmann, Opt. Commun. **7**, 163 (1990); S. A. Pikuz, T. A.

Shelkovenko, V. M. Romanova, D. A. Hammer, A. Ya. Faenov, V. A. Dyakin and T. A. Pikuz, in: *Soft X-Ray Lasers and Applications*, edited by J. J. Rocca and P. L. Hagelstein, Proc. SPIE **2520**, 330 (1995); Rev. Sci. Instrum. **68,** 740(1997).

[32] Y. Aglitskiy, T. Lehecka, A.Deniz, J. Hardgrove, J. Seely, C. Brown, U. Feldman, C. Pawley, K. Gerber, S. Bodner, S. Obenschain, R. Lehmberg, E. MacLean, M. Pronko, J. Sethian, A. Schmitt, C. Sullivan, G. Holland and M. Laming, Phys. Plasmas **3**, 3438 (1996)

[33] J. D. Sethian, S. E. Bodner, D. G. Colombant, J. P. Dahlburg, S. P. Obenschain, C. J. Pawley, V. Serlin, J. H. Gardner, Y. Aglitskiy, Y. Chan, A. V. Deniz, T. Lehecka, and M. Klapisch, Phys. Plasmas **6**, 2089 (1999).

[34] C. Pawley and A. V. Deniz, Rev. Sci. Instrum. **71**, 1286 (2000).

[35] J. P. Boris and D. L. Book, J. Comput. Phys. **11**, 38 (1973), also see "Solution of the Continuity Equation by the Method of Flux-Corrected Transport," *Methods in Computational Physics*, v. 16 (Academic Press, New York, 1976), pp. 85-129.